Cross Flows in the Taiwan Strait in Winter*

L.-Y. OEY

National Central University, Zhongli, Taiwan, and Princeton University, Princeton, New Jersey

Y.-L. CHANG

National Taiwan Normal University, Taipei, Taiwan

Y.-C. LIN AND M.-C. CHANG

National Central University, Zhongli, Taiwan

S. VARLAMOV AND Y. MIYAZAWA

Japan Agency for Marine-Earth Science and Technology, Yokosuka, Kanagawa, Japan

(Manuscript received 30 May 2013, in final form 10 September 2013)

ABSTRACT

In winter, a branch of the China Coastal Current can turn in the Taiwan Strait to join the poleward-flowing Taiwan Coastal Current. The associated cross-strait flows have been inferred from hydrographic and satellite data, from observed abundances off northwestern Taiwan of cold-water copepod species *Calanus sinicus* and, in late March of 2012, also from debris found along the northwestern shore of Taiwan of a ship that broke two weeks earlier off the coast of China. The dynamics related to such cross flows have not been previously explained and are the focus of this study using analytical and numerical models. It is shown that the strait's currents can be classified into three regimes depending on the strength of the winter monsoon: equatorward (poleward) for northeasterly winds stronger (weaker) than an upper (lower) bound and cross-strait flows for relaxing northeasterly winds between the two bounds. These regimes are related to the formation of the stationary Rossby wave over the Changyun Ridge off midwestern Taiwan. In the weak (strong) northeasterly wind regime, a weak (no) wave is produced. In the relaxing wind regime, cross-strait currents are triggered by an imbalance between the pressure gradient and wind and are amplified by the finite-amplitude meander downstream of the ridge where a strong cyclone develops.

1. Introduction

In winter, a narrow streak of cold coastal water is often seen in satellite imagery along the coast of China (Ning et al. 1998; Hickox et al. 2000; Hwang and Wong 2005; Chang et al. 2006). The China Coastal Current[1] stretches from the Yellow and East China Seas through the Taiwan Strait and, in some years of anomalously strong winter monsoon, as far south as Hainan Island in the South China Sea (Guan 1994; Guan and Fang 2006). Lin et al. (2005) and Pan et al. (2013) describe in situ observations for the portion of the current in the Taiwan Strait. These show that the current is generally equatorward, with speeds of $\sim$0.1–0.3 m s^{-1}, and has lower sea surface temperatures (SSTs $\approx$ 5°–20°C) and salinities S ($\approx$ 28–34 psu) than offshore.

The China Coastal Current contributes to fluxes of biogeochemical tracers, hence also to the biodiversity, of the China Seas (Liu et al. 2003; Liu 2013). The copepod species *Calanus sinicus*, for example, is widespread and peaks in spring–summer in the Yellow Sea (R. Wang et al. 2003; Zhang et al. 2007). Preferring temperate (10°–20°C) environments, *C. sinicus* drifts southward with the

[1] The current has different local names, for example, Zhemin Coastal Current in the Taiwan Strait (Hu et al. 2010).

* Supplemental information related to this paper is available at the Journals Online website: http://dx.doi.org/10.1175/JPO-D-13-0128.s1.

Corresponding author address: L.-Y. Oey, Atmospheric and Oceanic Sciences Program, 300 Forrestal Road, 114 Sayre Hall, Princeton University, Princeton, NJ 08540.
E-mail: lyo@princeton.edu

DOI: 10.1175/JPO-D-13-0128.1

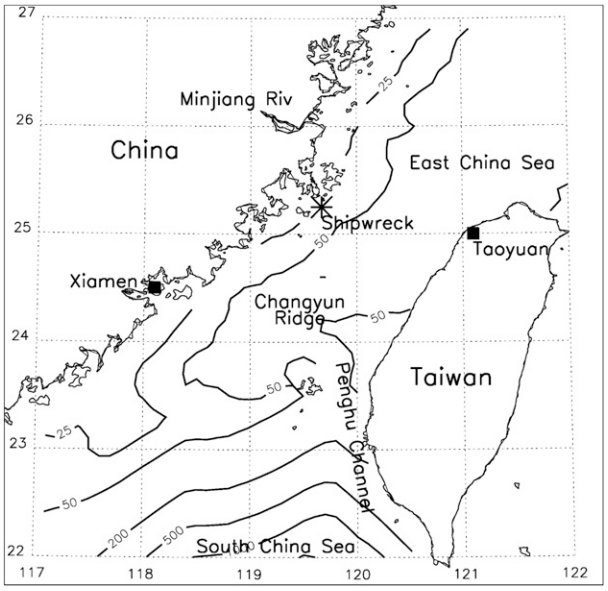

FIG. 1. Taiwan Strait location names and model isobaths (m). The domain is 22°–27°N and 117°–122°E.

China Coastal Current in winter, reaching as far south as the coastal waters of Hong Kong (Chen 1992; Hwang and Wong 2005). Interestingly, *C. sinicus* is also found during winter and early spring off the northwestern and northern coasts of Taiwan (Hwang and Wong 2005; Hwang et al. 2006). As *C. sinicus* is not endemic to the warm waters of Taiwan or the Kuroshio (Chen 1992) and the China Coastal Current is quite narrow, only about 30–50 km (Lin et al. 2005; Pan et al. 2013), the data suggest a cross-strait drift of *C. sinicus*, by some means or other, some 100 km across the Taiwan Strait. Because under winter's northeasterly winds the surface Ekman currents are directed toward China, they cannot explain the drift.

An incident that indicated cross-strait flow consistent also with the drift of *C. sinicus* occurred in late March of 2012. On 15 March 2012, in heavy seas under a strong northeasterly wind, a container ship went aground off the coast of China near 25.25°N, 119.67°E (Fig. 1; see http://www.mzwgk.gov.cn/show.aspx?id=3845&cid=37, which is in Chinese but includes the latitude/longitude of the shipwreck site), some 100 km northeast of the city of Xiamen; fortunately, the wind subsequently relaxed and the crews were rescued. Some 2 weeks later, on 31 March, some of the ship's debris was found on a beach in northwestern Taiwan near the city of Taoyuan. In this case, the origin and final point of the trajectory of the debris are known.

To understand dynamically how cross-strait flows occur is the main goal of this study. Numerical and analytical models in conjunction with the ship debris information, as well as vorticity and empirical orthogonal function (EOF) analyses, are used. Section 2 reviews the Taiwan Strait's circulation. In section 3, we use the currents from a numerical model of the North Pacific Ocean (Oey et al. 2013b) to calculate Lagrangian tracks of the shipwreck debris and use the information to validate the numerical model. We then derive an analytical classification of circulation regimes that depend on the strengths of the monsoon wind (section 4). We show that cross-strait flow under the wind relaxation regime is triggered by an imbalance between the along-strait pressure gradient and wind and amplified by the standing cyclone formed downstream of a topographic ridge off midwestern Taiwan. Section 5 examines time-dependent dynamics using the EOF; section 6 is the discussion and section 7 gives the conclusions.

2. Taiwan Strait circulation: An overview

The Taiwan Strait lies between mainland China (west) and Taiwan (east) (see Fig. 1); the averaged width is approximately 175 km and the length is about 350 km. The averaged depth between 23° and 25°N is about 50 m; the topography is generally shallower on the Chinese side of the strait, but is rather complicated. The strait was a low-lying plain some 17 000 years ago during the late Pleistocene when sea level was 100–140 m below the present (Fairbanks 1989; Voris 2000). A deep submarine valley southwest of Taiwan (the Penghu Channel) juts northward onto a ridge [the southern face of Changyun Ridge (henceforth CYR), approximately outlined by the 50-m isobath]; it then turns westward just north of Penghu Island to merge in the middle of the strait with another submarine valley (the Minjiang Trough)—believed to be the relict of an ancient river streaming down from the present day's Minjiang River, China (Boggs et al. 1979). The strait connects to the broad shelves of the East China Sea and South China Sea in the northeast and southwest, respectively. Across the shelf break in the south, the topography slopes steeply to a depth of 2000–3000 m into the South China Sea (Yu and Chou 2001).

Currents in the Taiwan Strait are influenced by the East Asian monsoon, which is northeasterly from September to April and southwesterly from May to August, as well as by open-ocean forcing (e.g., the Kuroshio); see Y. H. Wang et al. (2003) for a succinct summary and Hu et al. (2010) for a review of the circulation in the strait. Y. H. Wang et al. (2003; see also Liang et al. 2003) estimated a mean poleward transport of approximately 1.8 Sverdrups (Sv; $1\,\mathrm{Sv} \equiv 10^6\,\mathrm{m^3\,s^{-1}}$), stronger in summer, about 2.7 Sv, and weaker in winter, about 0.9 Sv; a poleward transport exists in the absence of wind, which

the authors suggested was induced by sea surface sloping down toward the north. Yang (2007) showed how such a slope may originate from the Kuroshio. Using a numerical model of the western North Pacific, Wu and Hsin (2005) estimated a transport ≈ 2 Sv driven by the surface slope, and their result suggests a transport reversal for northeasterly wind stronger than about $0.2\,\mathrm{N\,m^{-2}}$. Transport reversals were observed by Ko et al. (2003) who show that both local and remote winds (from farther north) contribute. Measurements by Lin et al. (2005) in October–December 1999 yielded a mean $\approx 0.12 \pm 0.33$ Sv, that is, poleward though not significantly different from zero, and a persistent northward flow was observed in the Penghu Channel southwest of Taiwan. In contrast, near the Chinese coast, the mean current was equatorward, approximately $-0.15\,\mathrm{m\,s^{-1}}$ near the surface at mooring C1 (25°N, 119.5°E). Off the Chinese coast near 25.6°N, 119.7°E, the measurements of Pan et al. (2013) also show a mean (February–March 2007) equatorward velocity of around $-0.2\,\mathrm{m\,s^{-1}}$ near the surface (15 m).

Besides the along-strait currents described above, wintertime cross-strait flows are seen in some hydrographic and satellite observations. Jan et al. (2002) mentioned hydrographic observations in various seasons during 1985–92 on Taiwan's side of the strait. No composites were shown; instead a 5-day survey from 12 to 16 November 1988 was reported as being typical of the winter monsoon season. On the northern face of CYR, the data show temperature T and salinity fronts: cooler and less saline waters of China Coastal Current origin on the northern side of the front and warmer and salty waters of mixed South China Sea–Kuroshio origin on the southern side. The T and S are vertically homogeneous, and they nearly compensate in density with the salinity being slightly more dominant, which agrees with the surveys of Li et al. (2006) and Pan et al. (2013). As the density is slightly lighter north than south of the front, a flow driven by the density gradient alone would be westward, opposite to the cyclonic sense required for *C. sinicus* or debris to drift from China to Taiwan; this suggests that frontogenesis is produced by other means. Li et al. (2006) showed similar cross-strait fronts from hydrographic and satellite SST data in winters, as did Chang et al. (2006, 2009), and noted that the fronts were highly variable. Numerical models by Wu et al. (2007), Yu et al. (2012), and Liao et al. (2013) show various patterns of cross-strait currents.[2]

[2] The earlier model by Jan et al. (2002), while instructive, is limited to the Taiwan Strait only; the numerical solution was strongly constrained by the open boundary conditions specified north and south of the strait.

3. Numerical simulation and validation of currents from winter to spring of 2012

Despite the above efforts of both observations and modeling, a dynamical explanation of how cross-strait flows can occur has so far not been presented in the literature. This study provides an explanation based in part on the analyses of simulated currents obtained from a North Pacific Ocean model. This section validates the model through particle trajectory simulation of the shipwreck debris, knowing the beginning and end dates and locations of the debris. The model is extensively described in Oey et al. (2013b); additional details are given in appendix 1 of the supplemental material. Briefly, the model is based on the Princeton Ocean Model (POM) covering the North Pacific Ocean from 16°S to 70°N and from 98°E to 73°W at $0.1° \times 0.1°$ horizontal resolution and with 41 terrain-following (sigma) levels. Satellite data are assimilated in the open ocean where depths exceed 1000 m to estimate T and S due to mesoscale features. No assimilation is done on shallow shelves including the Taiwan Strait, the dynamics of which then evolve according to the model physics and forcing across the shelf break by, for example, the Kuroshio and eddies (e.g. Chang and Oey 2011). Across the sea surface, 6-hourly National Centers for Environmental Prediction (NCEP) surface fluxes (wind, heat, and mass) are specified. A 24-yr unassimilated run from 1988 to 2011 forced also by NCEP surface fluxes provides the initial conditions for the more realistic assimilated run from 1 January 2012 to present. The model results from February to May 2012 (which includes the shipwreck period) are used for analyses and to derive analytical parameters for classification of current patterns in the strait.

Tracking shipwreck debris: 15 ~ 31 March 2012

Figure 2 shows modeled sea surface height (SSH) η and currents (u, v) (Fig. 2a) and the time series of the along-strait component of the wind stress τ^{oy} (kinematic, i.e., stress divided by the water density ρ_o) (Fig. 2b). Here, (x, y) is rotated 30° clockwise from true north with positive x and u (y and v) pointing cross strait (along strait) approximately southeastward (northeastward). The two dotted lines in the τ^{oy} plot delineate three circulation classes derived below: strong $\rho_o\tau^{oy} < -0.12\,\mathrm{N\,m^{-2}}$, moderate (or relaxation) $-0.12 < \rho_o\tau^{oy} < -0.068\,\mathrm{N\,m^{-2}}$, and weak $\rho_o\tau^{oy} > -0.068\,\mathrm{N\,m^{-2}}$. Winds were generally strong prior to the accident (before 15 March) when the strait's currents were predominantly southwestward (e.g., Fig. 2; 11 March), moderate during the drift of debris when a cross-strait cyclonic circulation developed north of the CYR (Fig. 2; 15 and 22 March), and weak thereafter when currents became generally northeastward (Fig. 2; 31 March).

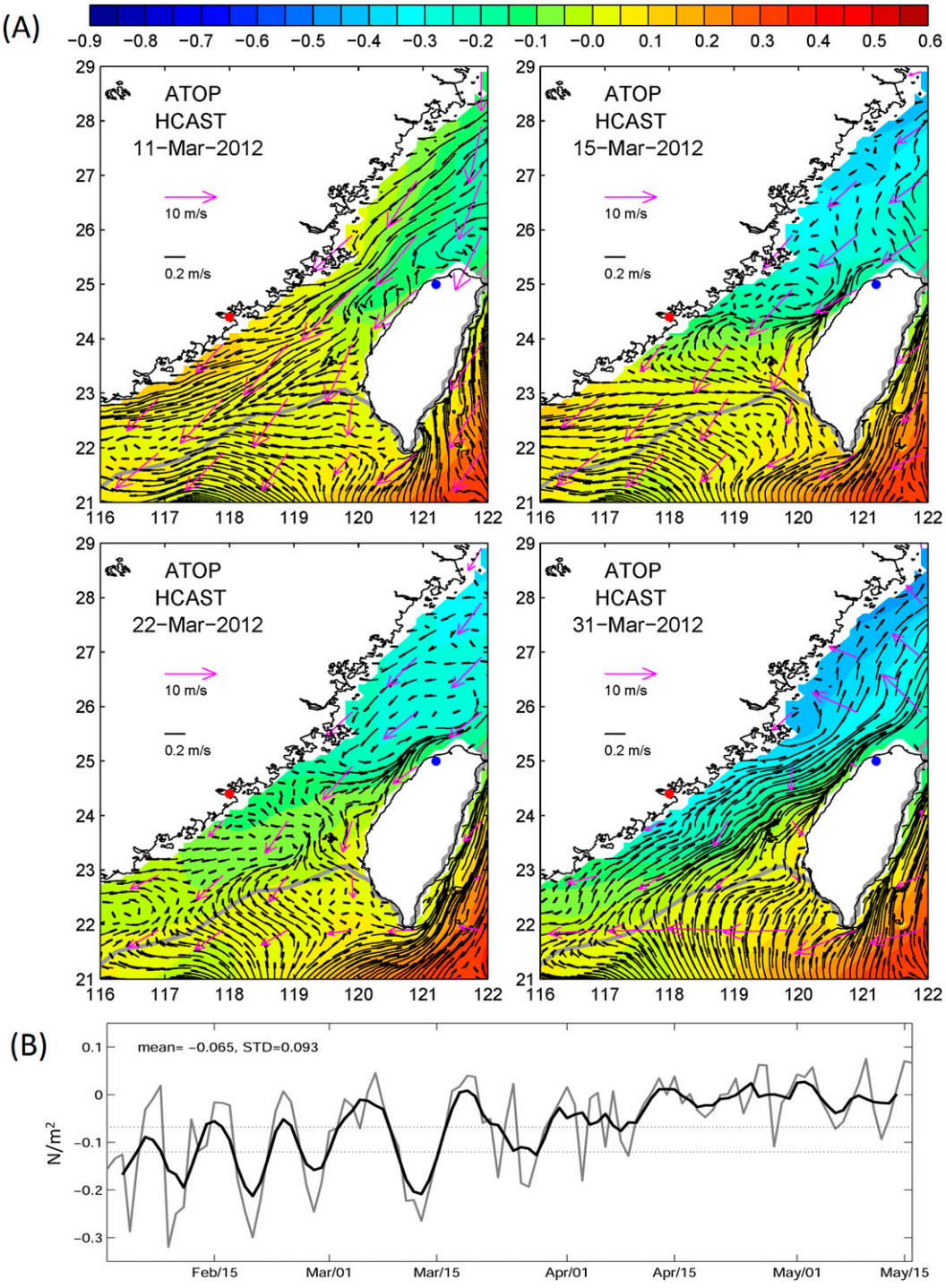

FIG. 2. (a) Model SSH (color; m) and currents at the indicated dates. Winds are shown as purple vectors. A 40-h Lanczos low-pass filter has been applied. Gray contour = 200-m isobath. For reference, red and blue dots mark Xiamen (China) and Taoyuan (Taiwan), respectively. The domain is 21°–29°N and 116°–122°E. (b) Along-strait wind stress (N m^{-2}; strait area averaged; mean and std dev are shown) from 15 Feb to 15 May: daily (gray) and 5 day averaged (black). Dotted lines are $\rho_o \tau^{oy} = -0.12$ and $\rho_o \tau^{oy} = -0.068$ N m^{-2} (see text).

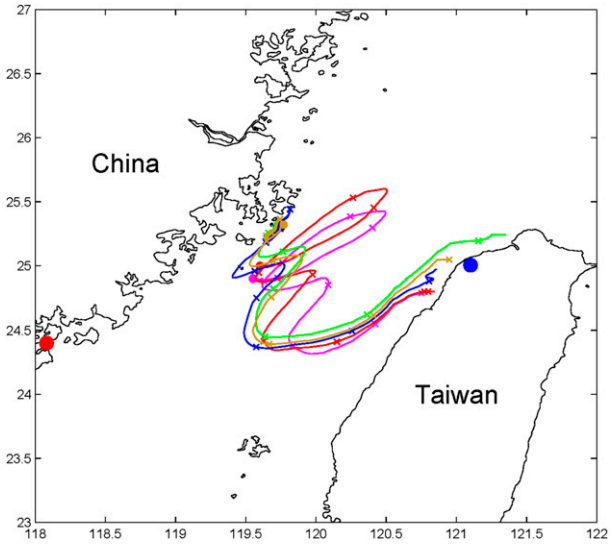

FIG. 3. Examples of trajectories of particles (different colors) released near Taoyuan (blue dot) on 31 Mar 2012, and tracked backward through 15 Mar. Trajectories are marked every 2 days by a cross. A red dot marks the city of Xiamen. The domain is 23°–27°N and 118°–122°E.

To assess the realism of the model currents, Lagrangian particles are tracked knowing the beginning and end locations and times of shipwreck debris. The position of a marked particle is tracked from its position $\mathbf{x}_o$ at time t_o to a new position $\mathbf{x} = \mathbf{x}_o + \Delta\mathbf{x}$ at time t (Awaji et al. 1980; Lin et al. 2007; Chang et al. 2011):

$$\mathbf{x}(\mathbf{x}_o, t) = \mathbf{x}_o + \int_{t_o} \mathbf{u}(\mathbf{x}_o, t')\, dt' + \int_{t_o} \left\{ \int_{t_o} \mathbf{u}(\mathbf{x}_o, t'')\, dt'' \cdot \nabla \mathbf{u}(\mathbf{x}_o, t') \right\} dt', \quad (3.1)$$

where the outer integral is from t_o to t, and the inner integral is from t_o to t'. The first integral is the Eulerian part, while the curly brackets within the second integral is the correction to $\mathbf{u}$ as the particle moves across $\Delta\mathbf{x} = \int_{t_o} \mathbf{u}(\mathbf{x}_o, t'')\, dt''$, integrating from t_o to t'. Figure 3 shows particles tracked backward (integrating with a negative time step) starting from locations near Taoyuan on 31 March 2012 when debris was found. Particles' positions on 15 March coincide well with the shipwreck site near 25.25°N, 119.67°E. As a check, we also verified that forward integration gave indistinguishable tracks. After the shipwreck, the simulated debris first drift southwestward and some make loops in the southwest–northeast direction nearly parallel to the Chinese coast before drifting southward to the center of the Taiwan Strait. There they turn rapidly eastward, then northeastward toward Taoyuan near the end of March.

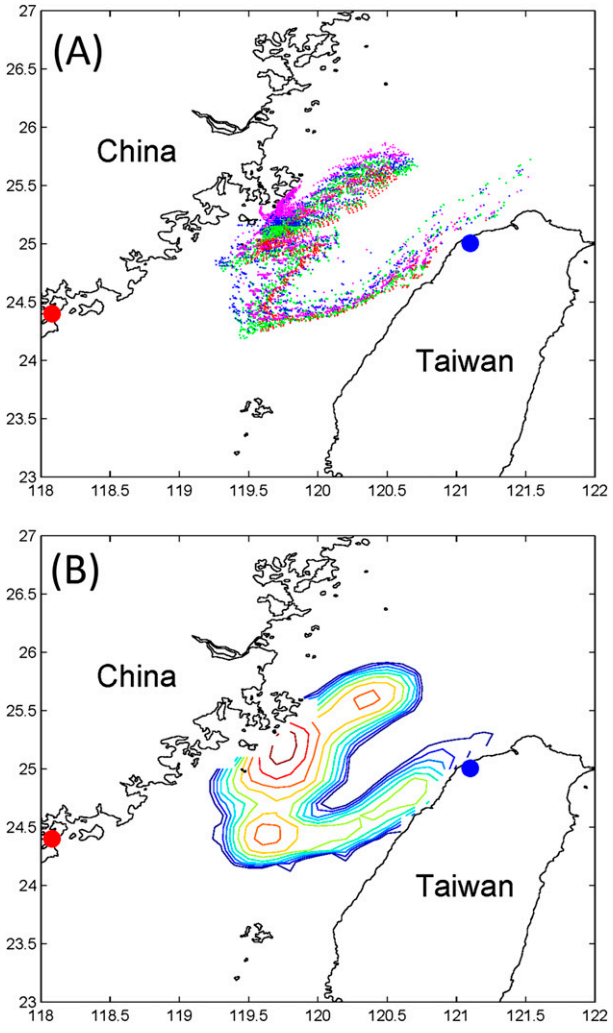

FIG. 4. (a) Positions of particles from 15 to 31 Mar 2012, all released at locations near the shipwreck site (25.25°N, 119.67°E); see text for details. (b) VF (arbitrary scale) shown as $\log_{10}(\mathrm{VF} \times 10)$; contour interval is 0.15 starting from 0.05. Red and blue dots mark Xiamen (China) and Taoyuan (Taiwan), respectively. The domain is 23°–27°N and 118°–122°E.

These tortuous trajectories reflect the complex spatiotemporal variability of the simulated currents.

To check the robustness of the simulated trajectories, sensitivity to the release location and time (due to, e.g., errors from finite-difference grid and model forcing) is assessed by tracking 120 particles starting at the shipwreck site and eight surrounding grid points on 15 March and 15 March ±6 h (Fig. 4a). We calculate the visitation frequency (VF) (Csanady 1983; Chang et al. 2011), defined as the number of times a chosen area (0.3° × 0.3° is used) is visited by the simulated particles as a percentage of the total number released (Fig. 4b). Particles generally disperse as described previously in Fig. 3; their paths connect shipwreck and landing sites in

loops and turns that are generally cyclonic and confined north of CYR. The VF shows a maximum close to the shipwreck site and two other local maxima: near 25.6°N, 120.3°E and 24.4°N, 119.6°E, which are choke points where the particles necessarily pass. For releases farther than the eight surrounding points and longer than ±6 h (not shown), particles spread south as well as north of the strait, but none come near Taoyuan. Therefore, while the actual paths of the debris are unknown, the model shows skill in correctly hindcasting the beginning and end locations of trajectories within a rather tight spatiotemporal window.

4. Flow patterns

The circulation on 15 March (Fig. 2a) suggests a Gill (1982, chapter 10)-type rotational dam-break solution consisting of Kelvin wave coastal currents on both sides of the strait joined by a cross-flow in the middle. Thus, as the northeasterly wind weakens, water surges northeastward due to higher SSH in the south than north of the strait. Stratification is weak during winter (Jan et al. 2002; Li et al. 2006; Pan et al. 2013) and in the presence of strong tides (Lefevre et al. 2000). Depth-independent currents were observed by Lin et al. (2005) and seen in model simulations by Wu et al. (2007), as well as in our model. To simplify, a homogeneous ocean is assumed and analytical formulae are derived to classify composite flow patterns dependent on the wind states. We then examine the depth-averaged vorticity balance.

a. Surface circulation

The forcing consists of wind at subtidal time scales from days to 1 ~ 2 weeks and along-strait sea level gradient $\partial\eta/\partial y$ at time scales of months and longer. The process is analyzed in terms of surface Ekman dynamics and frictionally controlled depth-averaged along-strait flow in a channel of constant depth H_o. Details are in appendix 2 of the supplemental material. The depth-averaged along-strait velocity v_A is

$$rv_A = -g\partial\eta/\partial y + \tau^{oy}/H_o, \tag{4.1}$$

where bottom friction is parameterized as $\boldsymbol{\tau}_b = rH_o\mathbf{u}_A$, r is the constant friction coefficient (s^{-1}), and $H_o = 50$ m is the strait's averaged depth. The r and $\partial\eta/\partial y$ are determined by regressing the numerically simulated v_A against τ^{oy}:

$$r \approx 1.66\times10^{-5}\,s^{-1} \quad \text{and} \quad \partial\eta/\partial y \approx -4.5\times10^{-7}. \tag{4.2}$$

Note that $\partial/\partial t \ll r^{-1}$ for subtidal flows, which justifies a priori the assumption in Eq. (4.1). Both values agree well with the corresponding values of $r \approx 1.65\times10^{-5}\,s^{-1}$ and $\partial\eta/\partial y \approx -3.8\times10^{-7}$ obtained in Wu and Hsin (2005) using a different model. Similar values of these parameters are also obtained using the results of the long-term unassimilated run (see the online supplemental material).

By incorporating the surface Ekman current, a critical τ^{oy} ($=\tau_v^{oy}$), when the along-strait component v_o of the surface velocity vanishes, is obtained:

$$\tau_v^{oy} \approx -1.2\times10^{-4}\,m^2\,s^{-2}. \tag{4.3a}$$

A similar analysis yields the critical τ_u^{oy} when the cross-strait surface velocity u_o vanishes:

$$\tau_u^{oy} \approx -0.68\times10^{-4}\,m^2\,s^{-2}. \tag{4.3b}$$

Physically, for a given sea level tilt, a stronger critical northeasterly wind stress ($\tau^{oy} < \tau_v^{oy}$) is necessary to maintain equatorward currents in the strait because bottom friction acts more effectively along strait than cross strait, because $|\tau_b^y| \gg |\tau_b^x|$. Because $\tau_v^{oy} < \tau_u^{oy}$, the same strong wind also forces cross-strait surface currents from Taiwan to China, that is, both v_o and $u_o < 0$; in this condition (e.g., 11 March; Fig. 2a), eastward drift of *C. sinicus* or debris is unlikely. At the other extreme when wind is weak (or southwesterly), $\tau_u^{oy} < \tau^{oy}$, the surface currents are northeastward toward Taiwan, that is, both v_o and $u_o > 0$ (e.g., 31 March, Fig. 2a); eastward drift exists, but particles are rapidly flushed into East China Sea by the strong along-strait flow. For moderate northeasterly wind stresses between these two critical values, that is, for $\tau_v^{oy} < \tau^{oy} < \tau_u^{oy}$, surface currents become complicated (e.g., 15 and 22 March; Fig. 2a), and additional analyses are necessary.

Figure 5 shows current and SSH composites based on the above classifications: strong wind pattern $\tau^{oy} < \tau_v^{oy}$ consisting of generally equatorward flow (Fig. 5a), weak wind pattern $\tau^{oy} > \tau_u^{oy}$ with generally poleward flow (Fig. 5c), and moderate wind pattern $\tau_u^{oy} > \tau^{oy} > \tau_v^{oy}$ that yields cross-strait flow north of CYR (Fig. 5b). Similar composite patterns are also obtained using the 24-yr unassimilated model data from 1988 to 2011 (not shown). Gill's solution applies during times of wind relaxation as flow surges northward;[3] its strength is estimated by repeating the analysis on a model run with constant shelf topography.[4] As shown in Fig. 5d, the solution consists of poleward coastal currents on both sides of the strait that are joined midstrait near 24.7°N by an eastward cross-flow

[3] A similar composite is also obtained using a more refined classification choosing only times when the wind relaxes (not shown).

[4] Water depth is set to 50 m for all shelf regions shallower than 200 m; a tanh function is used to produce a smooth transition from open-ocean topography to shelf.

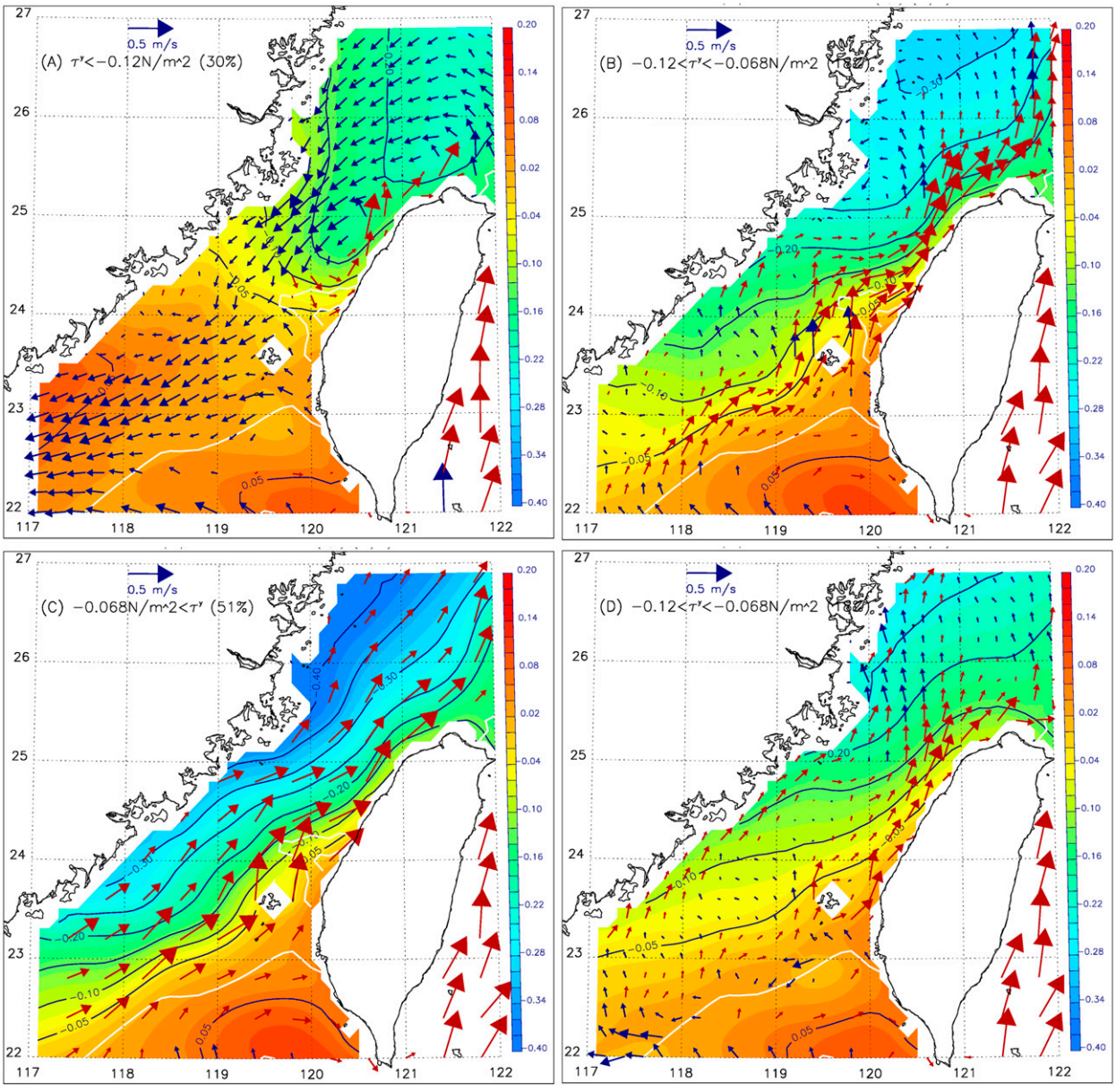

FIG. 5. Composite SSH (color and dark contours, m; SSH is omitted east of Taiwan for clarity) and surface currents for (a) strong, (b) moderate, and (c) weak along-strait wind (rotated 30° clockwise from true north, positive approximately northeastward). (d) As in (b), but for the constant shelf topography experiment. Wind ranges and percentages of each composite are shown. Outer isobaths 200 and 2000 m (barely seen) are shown as white contours, and the 35- and 50-m isobaths indicating the Changyuen Ridge in (a)–(c) are also plotted. Red (dark blue) vectors indicate currents with an eastward (westward) component. For clarity, vectors are drawn at every other grid on the shelves in (a),(b), and (d), and at every other two grids in (c) and also outside the shelves $H > 200$ m. The domain is 22°–27°N and 117°–122°E.

that, however, is weaker than the solution with topography (Fig. 5b).

b. Vorticity balance

To understand effects of topography on the cross-flow pattern of Fig. 5b, we examine the vorticity balance and isolate the process using an idealized model. The vorticity equation is derived from the equations of continuity and depth-averaged momentum:

$$\partial\eta/\partial t + \nabla\cdot(\mathbf{U}) = 0 \quad \text{and} \tag{4.4a}$$

$$\partial\mathbf{u}_A/\partial t + (\zeta + f)\mathbf{k}\times\mathbf{u}_A + \nabla(|\mathbf{u}_A|^2)/2 = -g\nabla\eta - \int_{-H}^{\eta}\int_{z}^{0}\nabla b\, dz'\, dz/D + (\boldsymbol{\tau}^o - \boldsymbol{\tau}_b)/D. \tag{4.4b}$$

Here, f is the Coriolis parameter, $\zeta = \mathbf{k}\cdot(\nabla\times\mathbf{u}_A)$ is the vertical component (unit vector $\mathbf{k}$ in z direction; $z = 0$ at

mean sea surface) of the curl of the depth-averaged velocity $\mathbf{u}_A = (u_A, v_A)$, $\mathbf{U} = D\mathbf{u}_A$ is the transport vector per unit length, $\nabla = (\partial/\partial x, \partial/\partial y)$ is the horizontal gradient operator, $b = g\rho/\rho_o$, ρ is the density, ρ_o is the reference density, H is the undisturbed water depth, η is the sea surface elevation, $D = H + \eta$ is the total water depth, and $\boldsymbol{\tau}^o$ and $\boldsymbol{\tau}_b$ are the (kinematic) wind and bottom stresses, respectively. Taking the curl, the z-component is (the z component is implied throughout the remaining of the paper)

$$\partial\zeta/\partial t + \mathbf{U}\cdot\nabla[(f+\zeta)/D] - [(f+\zeta)/D]\partial\eta/\partial t = J(\chi, D^{-1}) + \nabla\times[(\boldsymbol{\tau}^o - \boldsymbol{\tau}_b)/D], \tag{4.5a}$$

where $\chi = \int_{-H}^{\eta} zb\,dz'$ and $J(\chi, D^{-1}) = \partial\chi/\partial x\partial D^{-1}/\partial y - \partial D^{-1}/\partial x\partial\chi/\partial y$. The lhs is $D(\partial/\partial t + \mathbf{u}_A\cdot\nabla)(\mathrm{PV})$, where $\mathrm{PV} = (f+\zeta)/D$, so Eq. (4.5a) expresses PV conservation if the rhs = 0. Approximating $D \approx H$, and because in the composite $\partial\zeta/\partial t$ and $\partial\eta/\partial t$ are negligible, Eq. (4.5a) becomes

$$\underset{\mathrm{I}}{\mathbf{U}\cdot\nabla(f/H)} \approx \underset{\mathrm{II}}{-\mathbf{U}\cdot\nabla(\zeta/H)} \underset{\mathrm{III}}{-\nabla\times(\boldsymbol{\tau}_b/H)} \underset{\mathrm{IV}}{+J(\chi, H^{-1})} + \underset{\mathrm{V}}{\nabla\times(\boldsymbol{\tau}^o/H)}, \quad \text{for} \quad \chi \approx \int_{-H}^{0} zb\,dz', \tag{4.5b}$$

where roman numerals denote terms (with sign included) in the line above: I is the advection of background PV, II is the (minus) advection of relative PV or simply the nonlinear term, III is the minus curl of depth-distributed bottom stress, IV is the joint effect of baroclinicity and relief (JEBAR; Huthnance 1984; Mertz and Wright 1992), and V is the curl of depth-distributed wind stress; they are plotted in Figs. 6b–f for the moderate wind composite. Without II, Eq. (4.5b) corresponds to the linearized vorticity equation of the depth-averaged flow often used in the analysis of larger-scale dynamics, for which the JEBAR term is often discussed (e.g., Salmon 1992; Kagimoto and Yamagata 1997; Guo et al. 2003; Oey et al. 2010; Xu and Oey 2011). While I and II together express PV conservation (if I + II = 0), the other terms III, IV, and V represent different processes that modify PV. Equation (4.5b) is analogous to the classical Sverdrup balance, with $fH\nabla H^{-1}$ being the topographic beta (Pedlosky 1979) $\beta_T = fH\partial H^{-1}/\partial n$, where n is directed toward positive ∇H^{-1} (i.e., shallow depth), and it dominates the planetary beta $\beta = \nabla f$ in a small domain with significant topographic gradients. When the rhs = 0, $\mathbf{U}\cdot\nabla(f/H) \approx 0$ for barotropic geostrophic flow on f/H contours (Pedlosky 1979). Otherwise, $\mathbf{U}\cdot\nabla(f/H)$ is positive (negative) for upslope (downslope) transport. Figure 6a plots the $\mathbf{u}_A$ on f/H contours, showing vectors crossing f/H contours. As no f/H contours cut across the strait, any cross-strait flow is necessarily ageostrophic; the strength is calculated from I (Fig. 6b), which is contributed from II to V (Figs. 6c–f).

c. Balance north of the CYR

It is clear that over and downstream of the CYR, $-\mathbf{U}\cdot\nabla(\zeta/H)$ (Fig. 6c, note minus sign) dominates other ageostrophic terms and is generally of the same sign as $\mathbf{U}\cdot\nabla(f/H)$. McCartney (1975) shows that a standing Rossby wave of finite amplitude can be produced for prograde flow against the wave direction; such a wave is an idealization of the large-scale undulations in the westerly winds in midlatitudes, with low pressure anomalies in the lee of the Himalayan and Rocky Mountains (e.g., Lau 1979). In the Taiwan Strait (and East China Sea), topographic Rossby waves propagate southwestward and may be similarly arrested by a northeastward current. The wavelength is (Pedlosky 1979)

$$\lambda = 2\pi(V/\beta_T)^{1/2}, \tag{4.6}$$

where $V \approx 0.2\,\mathrm{m\,s^{-1}}$ is the speed of the current, and $\beta_T \approx 2.7\times10^{-10}\,\mathrm{m^{-1}\,s^{-1}}$;[5] then $\lambda \approx 170\,\mathrm{km}$, which agrees with the simulated meander wavelength downstream of CYR (see Fig. 5b). For retrograde flow of the strong wind case (Fig. 5a), no wave develops. In the weak wind case (Fig. 5c), V is larger and λ increases like $V^{1/2}$ primarily in the along-shelf direction (the cross-shelf scale is limited by the shelf width),[6] the cross-shelf velocity is $\propto 1/\lambda$ (i.e., it is proportional to the along-shelf derivative of the streamfunction), the meander amplitude is reduced, and current undulation becomes more elongated along shelf (Fig. 5c).

McCartney (1975)'s inertial solution is for flow past an isolated cylinder in an unbounded domain. To demonstrate the stationary wave in a channel over a coastal ridge, we configure an idealized domain shown in Fig. 7. The H decreases linearly from south to north except for a Gaussian ridge that juts out from the southern coast; the $\beta_T \approx 2.7\times10^{-10}\,\mathrm{m^{-1}\,s^{-1}}$, the same as in Taiwan Strait. Flow is barotropic and a steady westward wind stress of magnitude $= 0.07\,\mathrm{N\,m^{-2}}$ is applied. The bottom friction is increased 50 times in the sponge zone to make the flow smooth near the eastern end of the

[5] The term $\beta_T \approx (f/H)\cdot(40\,\mathrm{m})/175\,\mathrm{km}$, where 40 m is the difference in water depth across the strait whose width ≈ 175 km. Take $f \approx 6\times10^{-5}\,\mathrm{s^{-1}}$ and $H \approx 50\,\mathrm{m}$ to yield $\beta_T \approx 2.7\times10^{-10}\,\mathrm{m^{-1}\,s^{-1}}$.

[6] As V increases, cross-strait tilt in sea surface increases by geostrophy, effectively increasing β_T (Pedlosky 1979), which tends to reduce λ. The correction is quite small, about 10%.

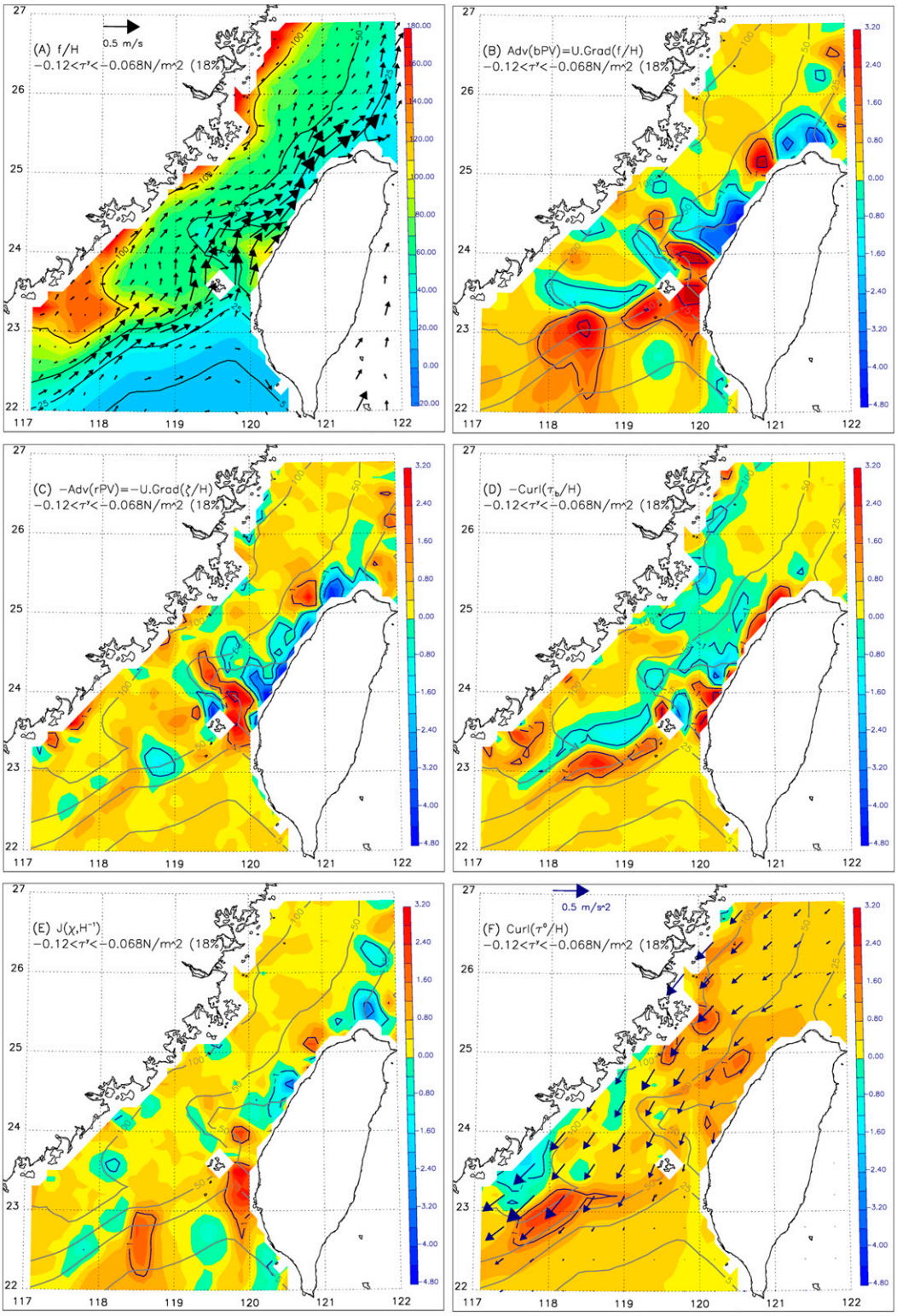

FIG. 6. Composite pattern ($\tau_v^{oy} < \tau^{oy} < \tau_u^{oy}$) of (a) depth-averaged currents (vectors drawn every other grid on shelves and every other two grids in deeper region) on f/H (color and contours, unit is $2 \times 10^{-8}\,\mathrm{m^{-1}\,s^{-1}}$; contour = 50 is $f/H = 10^{-6}\,\mathrm{m^{-1}\,s^{-1}}$; the contours approximately correspond to 30-, 60-, 120-, and 600-m isobaths; the CYR is outlined approximately by the 60-m contour inside which $f/H > 10^{-6}\,\mathrm{m^{-1}\,s^{-1}}$). Terms in the vorticity equation of the depth-averaged flow (see text; $10^{-10}\,\mathrm{s^{-2}}$): (b) $\mathbf{U} \cdot \nabla(f/H)$, (c) $-\mathbf{U} \cdot \nabla(\zeta/H)$, (d) $-\nabla \times (\boldsymbol{\tau}_b/H)$, (e) $J(\chi, H^{-1})$, and (f) $\nabla \times (\boldsymbol{\tau}^o/H)$; color (positive yellow–red) with contours are the vorticity terms, while the labeled gray contours are f/H. In (f) vectors are $(\boldsymbol{\tau}^o/H) \times 10^5$, thus scale shown is $= 5 \times 10^{-6}\,\mathrm{m\,s^{-2}}$. Penghu Island is at 23.6°N, 119.6°E. The domain is 22°–27°N and 117°–122°E.

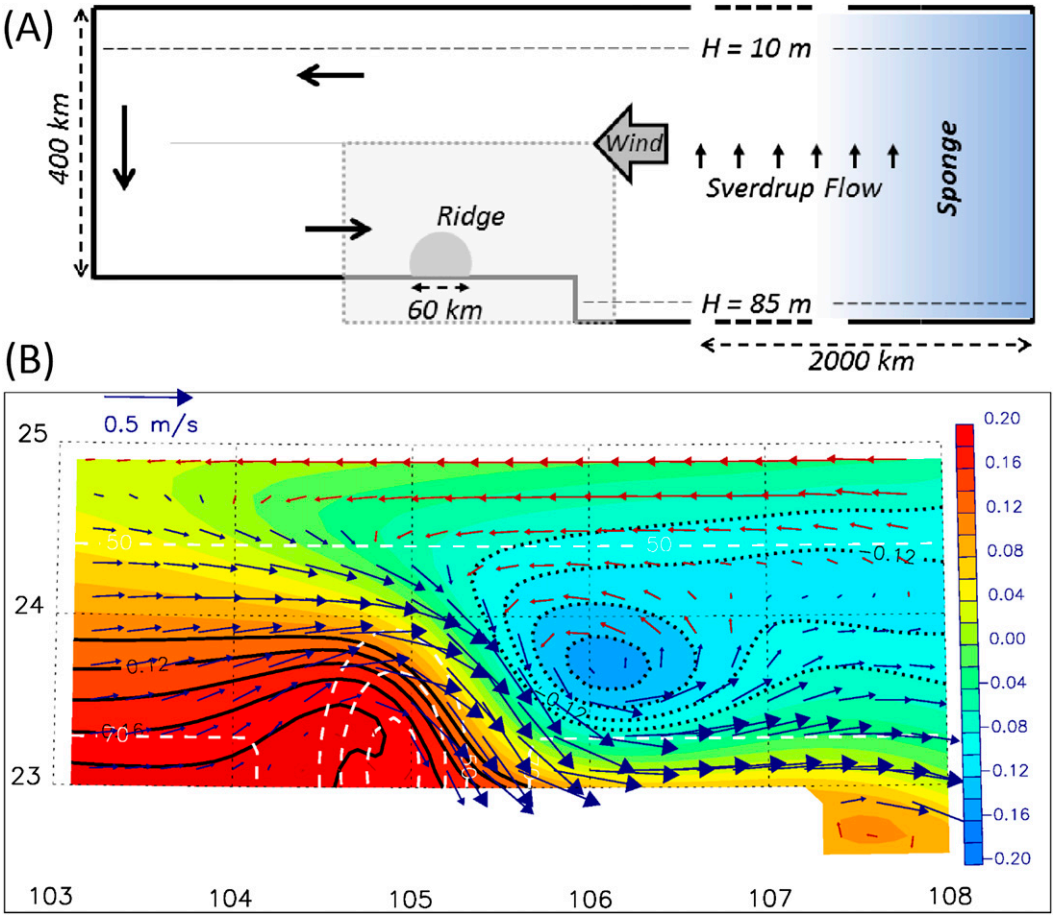

FIG. 7. (a) Model domain of a channel with y topographic gradient and ridge; horizontal scales are approximate. (b) SSH (color and dark contours, dotted if negative; m) and velocity (vectors, red for $u < 0$; m s^{-1}) for flow over a ridge inside the gray-shaded subdomain (~500 km × 200 km) shown in (a), with walls to the north (China; the thin gray line) and south (Taiwan). White dashed contours are isobaths = 70, 50, 40, and 30 m (on the ridge, radius ~30 km). The x and y axes are shown (°E and °N, respectively) though their values are arbitrarily chosen. McCartney (1975)'s bump and beta parameters, $h_o/(d\varepsilon)$ and $\beta_T L^2/V$, are 8 and 1.2, respectively.

channel. The wind produces a northward (topographic) Sverdrup flow (I and V balance), a southward boundary current at the western end of the channel, and a return eastward flow with speeds of about 0.2 m s^{-1} along the southern wall. The solution (Fig. 7) shows a standing wave with cyclone and anticyclone downstream of the ridge. McCartney (1975)'s solution also shows a cyclone–anticyclone pair.[7] However, because of the coast and the China Coastal Current, as well as friction, the present anticyclonic wave is weaker. There is a striking similarity of this idealized solution to Fig. 5b. We also confirm that when the background flow is stronger, the meander is elongated along shelf, while if the flow is reversed, no meander develops (not shown).

The standing wave cyclone contributes to the nonlinear term II that is strongly negative immediately downstream of the CYR, resulting in a downslope diabathic (i.e., across isobath) flow from China to Taiwan (Fig. 6c). Other weaker ageostrophic terms (III, IV, and V) contribute. Of these, $\nabla \times (\boldsymbol{\tau}^o/H)$ is externally imposed, while $J(\chi, H^{-1})$ and $-\nabla \times (\boldsymbol{\tau}_b/H)$ depend on the flow field. The JEBAR term (IV) arises because of parabathic (i.e., along isobath) density gradients. The density field varies slowly, O(months), consistent with the time scale for the Kuroshio, and the JEBAR term may therefore be considered given for nearly barotropic flows of O(days); JEBAR plots for the strong and weak wind cases (not shown) are in fact very similar to Fig. 6e.

[7] McCartney (1975)'s bump and beta parameters are $h_o/(d\varepsilon)$ and $\beta L^2/V$, respectively, where ε = Rossby number and $h_o/d \approx$ bump height/water depth. For CYR, the parameters are ≈ 8 and 1.2, respectively, corresponding approximately to his Fig. 4c.

JEBAR is generally weak [compared to, e.g., $\mathbf{U}\cdot\nabla(\zeta/H)$] in the northern half of the strait; it is negative immediately downstream of the CYR, tending to strengthen the cyclone. This downslope contribution to $\mathbf{U}\cdot\nabla(f/H)$ is because $\partial b/\partial x < 0$ along the northern (or southern) face of the CYR where $\partial H^{-1}/\partial y < 0$ (> 0) and $J(\chi, H^{-1})$ is negative (positive).[8] For the curl of the depth-distributed bottom stress (III), it may be considered a forcing of the interior flow through the Ekman layer paradigm (Ekman 1905; Pedlosky 1979). Figure 6d shows that $-\nabla\times(\boldsymbol{\tau}_b/H)$ is negative and contributes to a downslope diabathic current downstream of the CYR and over nearly the entire northern half of the strait. To understand, the term is split into three parts in Eq. (4.7) (plots not shown). Because $\boldsymbol{\tau}_b = C_d|\mathbf{u}_b|\mathbf{u}_b$,

$$\begin{aligned}-\nabla\times(\boldsymbol{\tau}_b/H) &= -\nabla\times[C_d|\mathbf{u}_b|(H^{-1})\mathbf{u}_b],\\ &= -C_d|\mathbf{u}_b|(H^{-1})\nabla\times\mathbf{u}_b - C_d|\mathbf{u}_b|\nabla(H^{-1})\\ &\quad\times\mathbf{u}_b - C_d(H^{-1})\nabla(|\mathbf{u}_b|)\times\mathbf{u}_b,\end{aligned} \tag{4.7}$$

where $\mathbf{u}_b$ is the near-bottom velocity, and $C_d \approx 2.5\times 10^{-3}$ is the bottom drag coefficient (Signell and Geyer 1991).[9] The third term is the "speed torque" and is small compared to the other two terms. The second term is $+\boldsymbol{\tau}_b\times\nabla(H^{-1})$, and it describes a "drag torque" on the water column due to larger drag in shallower water. As the column near the top (foot) of the ridge is dragged more (less), this term is dominant and negative immediately downstream of the CYR, forced by the strong cyclonic turning near the coast due to the stationary wave. The first term is vorticity dissipation that is negative downstream of the CYR; it in fact balances the wind torque. To see, we note that away from the strong cyclonic turning region, Figs. 6d and 6f indicate an approximate balance, $\nabla\times[(\boldsymbol{\tau}^o - \boldsymbol{\tau}_b)/H] \approx 0$. Therefore,

$$\begin{aligned}\nabla\times[(\boldsymbol{\tau}^o - \boldsymbol{\tau}_b)/H] &\approx \nabla\times(\boldsymbol{\tau}^o/H)\\ &\quad - C_d|\mathbf{u}_b|(H^{-1})\nabla\times\mathbf{u}_b \approx 0\end{aligned}$$

or,

$$r_b\zeta/H \approx H^{-1}\nabla\times\boldsymbol{\tau}^o - \boldsymbol{\tau}^o\times\nabla(H^{-1}). \tag{4.8}$$

Here, $C_d|\mathbf{u}_b|$ is approximated by a constant r_b, and $\nabla\times\mathbf{u}_b$ is approximated by ζ. Because the wind varies over a larger scale than the topography, the term involving $\nabla\times\boldsymbol{\tau}^o$ is small compared to the second term. For northeasterly wind, the wind torque $[-\boldsymbol{\tau}^o\times\nabla(H^{-1})$; Fig. 6f] therefore imparts a frictionally balanced cyclonic circulation.[10] This contribution enhances, but is clearly unrelated to, the cyclone produced by the stationary Rossby wave.

d. Balance south of the CYR

Here, Fig. 6b shows two bands where $\mathbf{U}\cdot\nabla(f/H)$ is negative, indicating likely sites of cross-strait flows from China to Taiwan. One band protrudes east-southeastward from 24.3°N, 118.6°E off the Chinese coast and terminates at Penghu Island. The other southern band along 23.5°N is blocked in the east by Penghu Island (23.6°N, 119.6°E) and by strong positive $\mathbf{U}\cdot\nabla(f/H)$ to the south and east of the island. These positive $\mathbf{U}\cdot\nabla(f/H)$ are due to $-\nabla\times(\boldsymbol{\tau}_b/H)$ and $J(\chi, H^{-1})$, with contribution from the depth-distributed wind stress $\nabla\times(\boldsymbol{\tau}^o/H)$ farther west near 118°E (see Figs. 6d–f). Figure 6e shows that JEBAR dominates over the outer shelf and shelf break ($f/H < 25$ contour or $H > 120$ m). As the Kuroshio makes a loop southwest of Taiwan, the mixed Kuroshio–South China Sea water interacts with cooler shelf waters west and north to produce onshelf intrusions along the Penghu Channel near 23°N, 120°E, as well as near 22.5°N, 118.5°E across the shelf break and continental slope (see Fig. 6b). These two intrusion locations coincide well with observed upwelling sites south of Penghu Island and Taiwan Bank (at 23°N, 118.5°E) (e.g., Hong et al. 2011). Farther inshore ($50 > f/H > 25$ contour or $60 < H < 120$ m), JEBAR weakens and $-\nabla\times(\boldsymbol{\tau}_b/H)$ becomes dominant (Fig. 6d). Here, the drag torque ($\boldsymbol{\tau}_b\times\nabla H^{-1}$; not shown) dominates on the seaward side because of the steep topography, contributing to a strong positive $-\nabla\times(\boldsymbol{\tau}_b/H)$, while the vorticity dissipation $[-C_d|\mathbf{u}_b|(H^{-1})\nabla\times\mathbf{u}_b]$ dominates on the shoreward side, contributing to a strong negative $-\nabla\times(\boldsymbol{\tau}_b/H)$; they give rise to the positive and negative bands, that is, convergence, as seen in Fig. 6d for $-\nabla\times(\boldsymbol{\tau}_b/H)$ across the outer shelf. It is interesting that, in spite of the fact that the wind is actually downwelling favorable, the above-mentioned upwelling south of the Taiwan Bank is produced by (i) JEBAR across the shelf break and (ii) convergence on the outer shelf caused by the drag torque and frictional spindown.

[8] Let x be along isobaths, $\partial H^{-1}/\partial y < 0$, and $b \approx b(x)$. Then $\nabla b = (\partial b/\partial x, 0)$, and $J(\chi, H^{-1}) \approx -(\partial b/\partial x)H^2(\partial H^{-1}/\partial y)/2$, which is negative (positive) if density decreases (increases) along the isobaths.

[9] In POM, C_d is not, strictly speaking, a constant, but the effect of a variable C_d is small. Also, because the flow is nearly barotropic in the strait, $\mathbf{u}_b \approx \mathbf{u}_A$; the argument is valid if $\mathbf{u}_b$ is replaced by $\mathbf{u}_A$.

[10] Approximating $\zeta \approx \partial v_A/\partial x$ and $H \approx H(x)$, the solution is $v_A = v_{A\text{China}} - \tau^{oy}\cdot\ln(H/H_{\text{China}})/r_b$, that is, cyclonic (anticyclonic) shear across the strait for $\tau^{oy} < 0$ (> 0). On the other hand, for constant H, Eq. (4.8) gives for positive $\nabla\times\boldsymbol{\tau}^o$ a cyclone with radial divergence (convergence) in the surface (bottom) Ekman layer (Pedlosky 1979).

5. Time-dependent dynamics

To understand time-dependent dynamics, we conduct EOF (Kutzbach 1967) analysis. Modes 1 and 2, discussed below, are found to be separated from their respective higher modes according to the criterion of North et al. (1982). Figure 8 shows EOFs 1 (Figs. 8a,b) and 2 (Figs. 8c,d) of SSH and surface current, analyzed for the period 1 February–15 May 2012 in the region shown in Fig. 8 (excluding the Kuroshio). The northeasterly monsoon ends near late April, and currents during the transition month of May contribute to the weak wind composite of Fig. 5c. The strait's transport is also plotted in Fig. 8 (red curve, time series). It is northeastward with a mean = 1.3 Sv that is between the estimates of 1.8 Sv by Y. H. Wang et al. (2003) and 1.09 Sv by Wu and Hsin (2005). Transport is weak in February, with a net ≈ 0 Sv consistent with Lin et al. (2005) mentioned previously, and is strong and northeastward (net ≈ 2.3 Sv) in May. Mode 1 accounts for 59% and 78% of the total variance for currents and SSH, respectively. The mode-1 principal components (PC1s; Figs. 8a,b, gray lines) show 3- $\sim$ 10-day events fluctuating about slower trends from winter to spring (thick black lines). The trends change from negative to positive in mid-March, which agrees with sign change in the transport anomaly. The PC1(η) and PC1(u, v) are significantly correlated: Corr[PC1(η), PC1(u, v)] = 0.94 (Table 1).[11] Their correlations with the along-strait wind stress are significant: Corr[PC1(η), τ^{oy}] = 0.83 and Corr[PC1(u, v), τ^{oy}] = 0.93 (Table 1). The corresponding eigenvectors (EV; i.e., spatial patterns), EV1(η) and EV1(u, v) indicate predominantly geostrophic along-strait flow balancing the cross-strait sea surface gradient. The EOF1s then describe responses to synoptic northeasterly winds that continually weaken from winter to spring, such that southwestward (northeastward) current anomalies accompany a higher (lower) η anomaly west than east of the strait.

Mode-2 EOFs account for about 10% of the total variance (Figs. 8c,d). The PC2(η) and PC2(u, v) are significantly correlated: Corr[PC2(η), PC2(u, v)] = 0.77 (Table 1). In contrast to EV1(η), whose structure is cross strait, EV2(η) shows a significant along-strait gradient (Fig. 8c). During the positive phase of PC2(η), the η anomaly is higher south than north of the strait. The southern high is largest at the southwestern end of the strait along the Chinese coast near 23°N, 117°E (SW High). The northern low is lowest at the northeastern end of the strait off northern Taiwan near 25°N, 121°E (NE Low). The corresponding EV2(u, v) in Fig. 8d shows that south of 22° $\sim$ 23°N, the SW-High together with the low in the South China Sea are in approximate geostrophic balance with the along-shelf current anomalies. North of 26° $\sim$ 27°N, in the East China Sea, the shelf flow anomaly is also in approximate geostrophic balance with EOF2(η). In contrast, inside the strait, the anomaly currents are ageostrophic. The current is poleward along the Chinese coast northeast of the SW-High. It turns eastward across the strait in the midstrait (24.5°N, 119°E) and continues cyclonically poleward off the northwestern coast of Taiwan toward the NE-Low. This ''N shape'' flow description fits well the surge pattern of Gill (1982), and the cyclone north of the CYR agrees with the stationary Rossby wave solution.

Though weaker than EOF1, the EOF2 is therefore crucial in explaining the cross-strait flow. From 15 to 31 March, the PC2s are generally positive, which, coupled with weakened PC1s during the same period, contribute to the cyclone north of the CYR, consistent with the Lagrangian paths after the shipwreck (Figs. 3 and 4). More generally, we note that both PC2(η) and PC2(u, v) are anticorrelated with τ^{oy}; the correlations are -0.68 and -0.52, respectively, with wind leading by 1 day (Table 1). As the northeasterly wind strengthens ($\tau^{oy} < 0$), sea level at the southern end of the strait (the SW High; Fig. 8c) rises. It becomes at maximum approximately 1 day after the peak wind, concomitant with the N-shape flow pattern inside the strait (Fig. 8d). Thus, EOF2 corresponds to the fluctuating part of the along-strait pressure gradient (PG) neglected in the analytical model, because the latter assumes that the pressure gradient is quasi steady. To quantify, we split the velocity into three parts:

$$\mathbf{u} \approx \mathbf{u}_{\mathrm{PG}} + \mathbf{u}_{\mathrm{wind}} + \mathbf{u}_{\mathrm{PG}'}. \tag{5.1}$$

Here, $\mathbf{u}_{\mathrm{PG}}$ is (quasi) steady due to large-scale pressure gradient forcing from outside the strait, $\mathbf{u}_{\mathrm{wind}}$ is due to the (fluctuating) wind, and $\mathbf{u}_{\mathrm{PG}'}$ is due to the fluctuating along-strait sea level gradient. The $\mathbf{u}_{\mathrm{PG}'}$ lumps together time-dependent processes that are otherwise locally driven by $\mathbf{u}_{\mathrm{wind}}$; it may include, among other processes, effects of sea level setup by, for example, coastal-trapped waves by remote wind (Ko et al. 2003). The splitting is simplistic for it neither accounts for other physics nor for potential interactions between them. We identify $\mathbf{u}_{\mathrm{PG}}$ + $\mathbf{u}_{\mathrm{wind}}$ with the analytical model for which the along-strait surface velocity is v_o. Thus, for the along-strait component

$$v_{o\mathrm{PG}'} \approx v_m - v_o, \tag{5.2}$$

[11] Here, the notation Corr(A, B, lags) = max lagged correlation coefficient between A and B with lags (days), positive (negative) if A leads (lags) B. All correlations quoted in this paper are above the 95% significance level. For simplicity, we write Corr(A, B) for the zero-lag correlation.

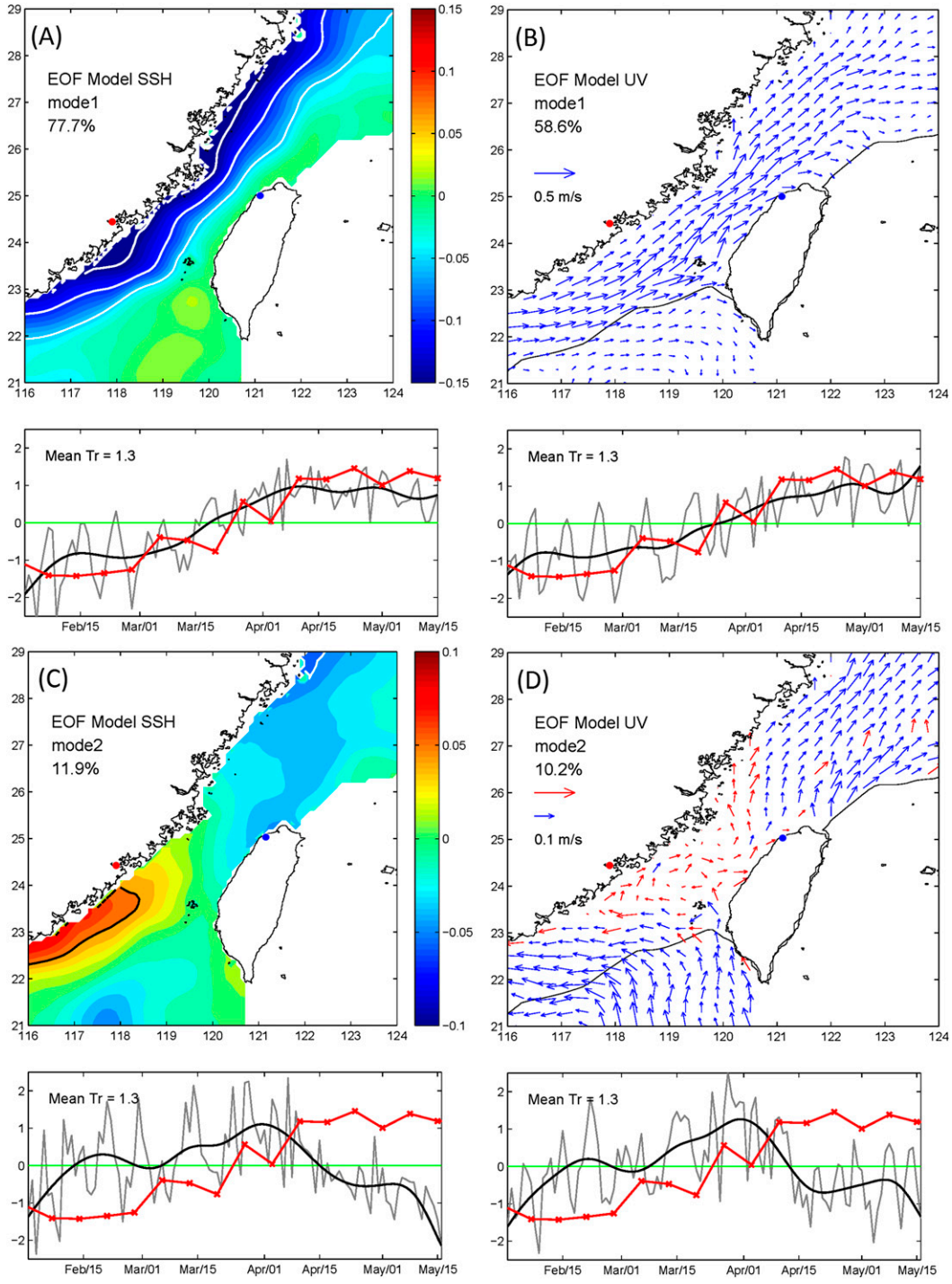

FIG. 8. EOF modes (a),(b) 1 and (c),(d) 2 for (left) SSH and (right) currents in the Taiwan Strait shown from 1 Feb to 15 May 2012. In each case, the spatial pattern (top; eigenfunction: m for SSH and m s^{-1} for velocity) and the principal components (bottom; nondimensionalized by respective std dev) are given for daily values (light line) and 10-day running mean (heavy line). Red curve is the weekly strait's transport anomaly (Sv) and its mean is printed (=1.3 Sv). Red vectors enlarge the mode-2 (u, v) scale in the strait.

TABLE 1. Correlations/lags (days; >0 if column 1 leads; 0 lags omitted) between variables in column 1 with those in row 1. Values shown are above the 95% significance level. Dash indicates insignificant correlation (at the 95% level). For each correlation, the 95% significance level is computed from $1 - (1\text{–}0.95)^{2/(F-1)}$, where F is the degrees of freedom calculated as N/τ_N, N is length of time series, and τ_N is the dot product of the autocovariances of the two time series.

	PC1(η)	PC1(u, v)	PC2(η)	PC2(u, v)	τ^{oy} or v_o	$v_{o\mathrm{PG}'}$	v_m
PC1(η)	1	0.94	—	—	0.83	—	0.93
PC1(u, v)	0.94	1	—	—	0.93	—	0.98
PC2(η)	—	—	1	0.77	−0.68/−1	0.70/−1	−0.35
PC2(u, v)	—	—	0.77	1	−0.52/−1	0.61/−1.5	—
τ^{oy} or v_o	0.83	0.93	−0.68/1	−0.52/1	1	−0.62	0.94
$v_{o\mathrm{PG}'}$	—	—	0.70/1	0.61/1.5	−0.62	1	−0.32
v_m	0.93	0.98	−0.35	—	0.94	−0.32	1

where v_m is the strait-averaged, along-strait surface velocity obtained from the numerical model. The v_m and v_o are highly correlated, which justifies a priori the above splitting (Fig. 9); in general, $v_m > v_o$, that is, $v_{o\mathrm{PG}'} > 0$. Physically, because the (magnitude of) sea level tilt included in v_o is a minimum [it is the zero intercept of the v_A–τ^{oy} regression from Eq. (4.1)], additional (fluctuating) tilts simulated by the numerical model (contained in v_m) always drive a more poleward current $v_{o\mathrm{PG}'}$. Moreover, because the fluctuations of v_o are entirely due to wind, its high correlation with v_m means that $v_{o\mathrm{PG}'}$ is also largely wind forced: Corr($v_{o\mathrm{PG}'}$, τ^{oy}) = −0.62 (Table 1). Thus, as the northeasterly wind strengthens ($\tau^{oy} < 0$), the component of the velocity that is driven by the fluctuating pressure gradient (i.e., $v_{o\mathrm{PG}'}$) is northeastward, opposing the wind. These results suggest that $v_{o\mathrm{PG}'}$ is related to EOF2. As shown in Table 1, while $v_{o\mathrm{PG}'}$ is not correlated with EOF1s, it is significantly correlated with both PC2(η) and PC2(u, v), with correlations 0.70 and 0.61, respectively, when $v_{o\mathrm{PG}'}$ leads by 1 ~ 1.5 days.[12] It is interesting that v_m correlates well with PC1s, but it (like PC1s) correlates poorly with PC2s. This is because EOF1 is geostrophic while EOF2 is ageostrophic, accounting for only ~10% of the total variance. By extracting the (large) part of v_m that is explained by the fluctuating winds (i.e., v_o) as done above, the remainder $v_{o\mathrm{PG}'}$ correlates well with the PC2s.

Summarizing, fluctuating wind drives the current anomaly that is predominantly along strait and in geostrophic balance with the cross-strait sea level gradient—this is mode 1. Pressure imbalances by the fluctuating wind are represented by mode 2; they drive ageostrophic "surge" currents ($v_{o\mathrm{PG}'}$) that are measured in Fig. 9b by the difference between the solid regression line and the 45° line. As $v_{o\mathrm{PG}'}$ is a strait-averaged quantity, it does not describe the details of the cross flows. However, it is clear from Fig. 8d that mode 2 encompasses both the surge and standing wave solutions. Cross-strait flow is thus initiated by a surge and then, as northeasterly wind weakens and along-strait flow turns poleward, is amplified by the excitation of the standing Rossby wave downstream of the CYR.

6. Discussion

Cross-strait flows may be related to the occurrences of fronts observed in the northern Taiwan Strait during winter and spring by Chang et al. (2006) and Li et al. (2006). Jan et al. (1998) noted that "...cold water bulge occupies the upper layer of the area north of the ridge..." and Jan et al. (2002) described "winter blocking" of the northward current by the CYR. Dynamically, blocking is caused by the Rossby wave drag that can be estimated by applying McCartney (1975)'s formula using parameters for the CYR, which yields $r_{\mathrm{wave}} \approx 0.6 \times 10^{-5}\,\mathrm{s}^{-1}$. This is about 1/3 of the r value obtained directly from the numerical model [Eq. (4.2)], suggesting that wave drag plays an important role in the Taiwan Strait.

It is clear that cross flows are episodic events and time dependent, as has been previously noted in observations (Li et al. 2006; Chang et al. 2006, 2009). Nonetheless, such events transport *C. sinicus* from the China Coastal Current to northwestern Taiwan and, as we have demonstrated, shipwreck debris as well during the 15–31 March 2012 event. For the winter–spring period of 2012, our model indicates that cross-flow events compose only 19%, while the equatorward and poleward events are 30% and 51%, respectively (Fig. 5); a similar percentage (approximately 20%) is also obtained in the 24-yr composite using the 1988–2011 nonassimilated run (not shown). These results are consistent with the relatively low

[12] The lead is explained as follows. Let $\mathrm{PG}' = g\partial\eta'/\partial y = \alpha_o e^{i\omega t}$, $\alpha_o \sim \tau^{oy}/H$, that is, northeasterly wind forces negative $\partial\eta'/\partial y$, where ~ means proportional to. The along-strait momentum with PG′ as forcing is then $\partial v_{o\mathrm{PG}'}/\partial t = -\alpha_o \cdot e^{i\omega t}$. Thus $v_{o\mathrm{PG}'} \sim \alpha_o \cdot e^{i(\omega t + \pi/2)}$, that is, it leads PG′ by $\pi/2$, or $\pi/2 + r/\omega$, $r/\omega \ll 1$ with friction r. If PG′ is identified as PC2(η), then $v_{o\mathrm{PG}'}$ leads PC2(η) also by at least $\pi/2$ or at least 1–1.5 days for wind periods of $2\pi/\omega \approx 4$–6 days (Fig. 2b).

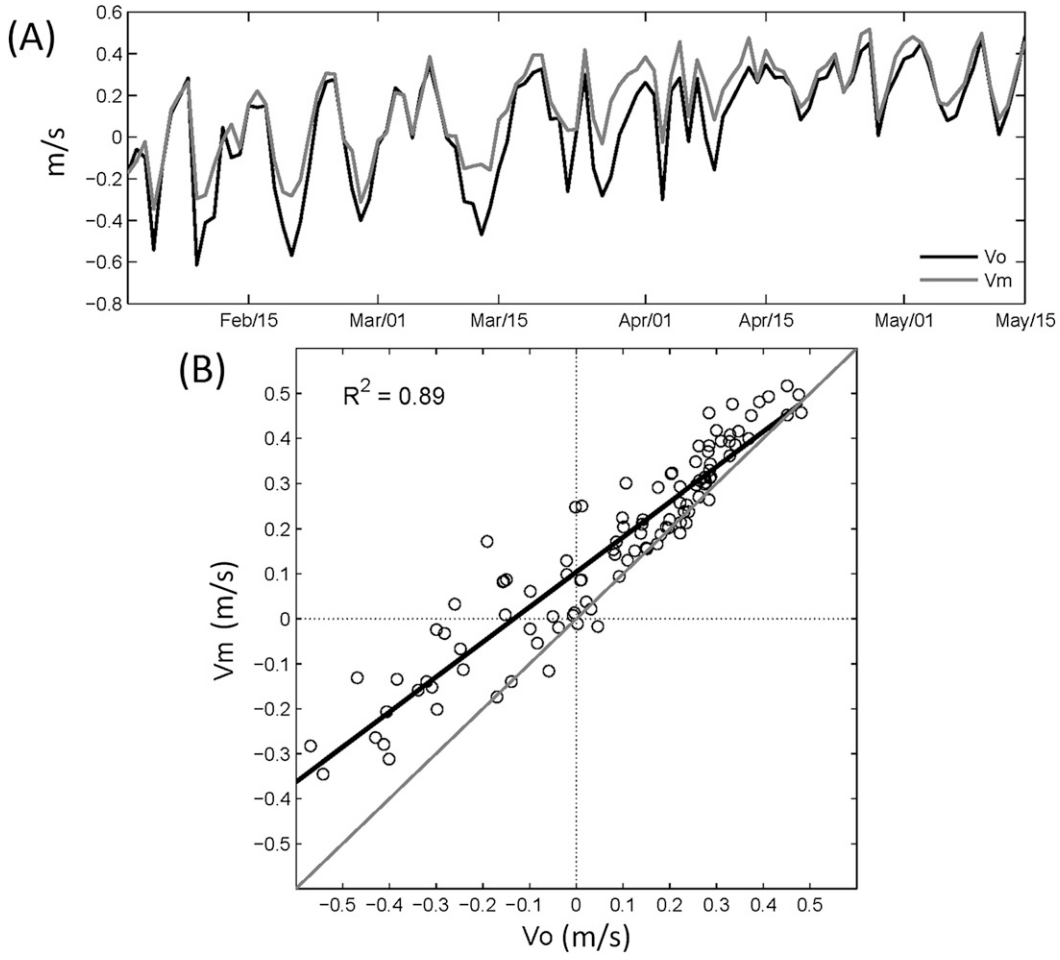

FIG. 9. (a) Time series of daily along-strait velocities v_o and v_m ($\mathrm{m\,s^{-1}}$) from the analytical and numerical models, respectively, and (b) their regression (thick line).

percentage of *C. sinicus* (compared to other copepod species) observed northwest of Taiwan during winter (Hwang et al. 2006).

Knowledge of the strait's currents can be applied to study not only of the dispersion of tracers, but also fish migratory patterns. Cross-strait currents probably do little in dictating the movement of fish. However, currents affect temperature and salinity upon which fish depend for their habitat and survival (Chang et al. 2004). Our research suggests that these can be profoundly affected from year to year by interannual changes in the strength of the monsoon wind that in turn alters the strait's circulation (cf. Chang et al. 2009). According to the present study, beacause cross flows depend on the existence of moderate wind and/or relaxation episodes of northeasterly wind exceeding a lower-bound threshold ($\rho_o \tau^{oy} < -0.068\,\mathrm{N\,m^{-2}}$), they would be more (less) frequent in La Niña (El Niño) years or during years of negative (positive) Philippines–Taiwan Oscillation (PTO) index (Chang and Oey 2012, see their Fig. 7) when the northeasterly monsoon wind tends to be strong (weak). This is in fact the case (Oey et al. 2013a) and it and other issues related to interannual variability of currents and distribution of marine organisms in the strait will be reported in a separate study.

7. Conclusions

This work attempts to explain how cross flows in the Taiwan Strait can develop in winter. The two main findings are as follows:

1) there exist three circulation regimes depending on the strength of the northeasterly wind: generally equatorward (poleward) along-strait flow for wind stronger (weaker) than an upper (lower) bound and cross-strait flow for moderate wind in between; and
2) cross-strait flow from China to Taiwan is triggered in the northern half of the strait by poleward surge of

flow as wind relaxes due to the imbalance between pressure gradient and wind forcing; the cross flow then strengthens downstream of a midstrait ridge as finite-amplitude cyclone of a stationary Rossby wave develops.

These conclusions are supported by composite and vorticity analyses; in particular, nonlinear inertial term dominates other ageostrophic terms in the region of the stationary wave north of the CYR. In the southern portion of the Taiwan Strait, across the shelf break of the South China Sea, the JEBAR and curl of the bottom stress explain the strong onshelf intrusions often observed during winter, despite the prevailing, downwelling-favorable northeasterly wind.

Acknowledgments. We thank two anonymous reviewers whose comments improved the manuscript. We thank Drs. Hwa Chien and K.-K. Liu (NCU) for informing us of the shipwreck incident, and Drs. Yan-Hua Zhang and Ping Chen for locating the accident site. LYO is grateful for the award from the Taiwan's Foundation for the Advancement of Outstanding Scholarship. The research is in part supported by the National Science Council, the Ministry of Education, and the National Central University, Taiwan.

REFERENCES

Awaji, T., N. Imasato, and H. Kunishi, 1980: Tidal exchange through a strait: A numerical experiment using a simple model basin. *J. Phys. Oceanogr.,* **10,** 1499–1508, doi:10.1175/1520-0485(1980)010<1499:TETASA>2.0.CO;2.

Boggs, S., Jr., W. C. Wang, F. S. Lewis, and J.-C. Chen, 1979: Sediment properties and water characteristics of the Taiwan shelf and slope. *Acta Oceanogr. Taiwan.,* **10,** 10–49.

Chang, C.-W., S.-H. Lin, Y. Lizuka, and W.-N. Tzeng, 2004: Relationship between Sr:Ca ratios in otoliths of grey mullet *Mugil cephalus* and ambient salinity: Validation, mechanisms, and applications. *Zool. Stud.,* **43,** 74–85.

Chang, Y., T. Shimada, M.-A. Lee, H.-J. Lu, F. Sakaida, and H. Kawamura, 2006: Wintertime sea surface temperature fronts in the Taiwan Strait. *Geophys. Res. Lett.,* **33,** L23603, doi:10.1029/2006GL027415.

——, K.-T. Lee, M.-A. Lee, and K.-W. Lan, 2009: Satellite observation on the exceptional intrusion of cold water in the Taiwan Strait. *Terr. Atmos. Oceanic Sci.,* **20,** 661–669, doi:10.3319/TAO.2008.08.07.01(Oc).

Chang, Y.-L., and L.-Y. Oey, 2011: Interannual and seasonal variations of Kuroshio transport east of Taiwan inferred from 29 years of tide-gauge data. *Geophys. Res. Lett.,* **38,** L08603, doi:10.1029/2011GL047062.

——, and ——, 2012: The Philippines–Taiwan Oscillation: Monsoonlike interannual oscillation of the subtropical–tropical western North Pacific wind system and its impact on the ocean. *J. Climate,* **25,** 1597–1618, doi:10.1175/JCLI-D-11-00158.1.

——, ——, F.-H. Xu, H.-F. Lu, and A. Fujisaki, 2011: 2010 oil spill: Trajectory projections based on ensemble drifter analyses. *Ocean Dyn.,* **61,** 829–839, doi:10.1007/s10236-011-0397-4.

Chen, Q. C., 1992: *Zooplankton of China Seas.* Vol. 1. Science Press, 87 pp.

Csanady, G. T., 1983: Dispersal by randomly varying currents. *J. Fluid Mech.,* **132,** 375–394, doi:10.1017/S0022112083001664.

Ekman, V. W., 1905: On the influence of the Earth's rotation on ocean-currents. *Arkiv for Matematik, Astronomi och Fysik,* **2** (11), 1–52.

Fairbanks, R. G., 1989: A 17,000-year glacio-eustatic sea level record: Influence of glacial melting rates on the Younger Dryas event and deep-ocean circulation. *Nature,* **342,** 637–642, doi:10.1038/342637a0.

Gill, A. E., 1982: *Atmosphere–Ocean Dynamics.* Academic Press, 662 pp.

Guan, B. X., 1994: Patterns and structures of the currents in Bohai, Huanghai and East China Seas. *Oceanology of China Seas,* Vol. 1, D. Zhou et al., Eds., Kluwer Academic Publishers, 17–26.

——, and G. H. Fang, 2006: Winter counter-wind currents off the southeastern China coast: A review. *J. Oceanogr.,* **62,** 1–24, doi:10.1007/s10872-006-0028-8.

Guo, X., H. Hukuda, Y. Miyazawa, and T. Yamagata, 2003: A triply nested ocean model for simulating the Kuroshio—Roles of horizontal resolution on JEBAR. *J. Phys. Oceanogr.,* **33,** 146–169, doi:10.1175/1520-0485(2003)033<0146:ATNOMF>2.0.CO;2.

Hickox, R., I. Belkin, P. Cornillon, and A. Shan, 2000: Climatology and seasonal variability of ocean fronts in the East China, Yellow and Bohai Seas from satellite SST data. *Geophys. Res. Lett.,* **27,** 2945–2948, doi:10.1029/1999GL011223.

Hong, H., F. Chai, C. Zhang, B. Huang, Y. Jiang, and J. Hu, 2011: An overview of physical and biogeochemical processes and ecosystem dynamics in the Taiwan Strait. *Cont. Shelf Res.,* **31,** S3–S12, doi:10.1016/j.csr.2011.02.002.

Hu, J., H. Kawamura, C. Li, H. Hong, and Y. Jiang, 2010: Review on current and seawater volume transport through the Taiwan Strait. *J. Oceanogr.,* **66,** 591–610, doi:10.1007/s10872-010-0049-1.

Huthnance, J. M., 1984: Slope currents and ''JEBAR''. *J. Phys. Oceanogr.,* **14,** 795–810, doi:10.1175/1520-0485(1984)014<0795:SCA>2.0.CO;2.

Hwang, J.-S., and C. K. Wong, 2005: The China Coastal Current as a driving force for transporting *Calanus sinicus* (Copepoda: Calanoida) from its population centers to waters off Taiwan and Hong Kong during the winter northeast monsoon period. *J. Plankton Res.,* **27,** 205–210, doi:10.1093/plankt/fbh162.

——, and Coauthors, 2006: A 5-year study of the influence of the northeast and southwest monsoons on copepod assemblages in the boundary coastal waters between the East China Sea and the Taiwan Strait. *J. Plankton Res.,* **28,** 943–958. [Available online at http://plankt.oxfordjournals.org/content/28/10/943.full.]

Jan, S., C.-S. Chern, and J. Wang, 1998: A numerical study of currents in the Taiwan Strait during winter. *Terr. Atmos. Oceanic Sci.,* **9,** 615–632.

——, J. Wang, C.-S. Chern, and S.-Y. Chao, 2002: Seasonal variation of the circulation in the Taiwan Strait. *J. Mar. Syst.,* **35,** 249–268, doi:10.1016/S0924-7963(02)00130-6.

Kagimoto, T., and T. Yamagata, 1997: Seasonal transport variations of the Kuroshio: An OGCM simulation. *J. Phys. Oceanogr.,* **27,** 403–418, doi:10.1175/1520-0485(1997)027<0403:STVOTK>2.0.CO;2.

Ko, D. S., R. H. Preller, G. A. Jacobs, T. Y. Tang, and S. F. Lin, 2003: Transport reversals at Taiwan Strait during October and November 1999. *J. Geophys. Res.,* **108,** 3370, doi:10.1029/2003JC001836.

Kutzbach, J., 1967: Empirical eigenvectors of sea level pressure, surface temperature, and precipitation complexes

over North America. *J. Appl. Meteor.,* **6,** 791–802, doi:10.1175/1520-0450(1967)006<0791:EEOSLP>2.0.CO;2.

Lau, N.-C., 1979: The observed structure of tropospheric stationary waves and the local balances of vorticity and heat. *J. Atmos. Sci.,* **36,** 996–1016.

Lefevre, F., C. Le Provost, and F. H. Lyard, 2000: How can we improve a global ocean tide model at a regional scale? A test on the Yellow Sea and the East China Sea. *J. Geophys. Res.,* **105** (C4), 8707–8725, doi:10.1029/1999JC900281.

Li, C., J. Hu, S. Jan, Z. Wei, G. Fang, and Q. Zheng, 2006: Winter–spring fronts in Taiwan Strait. *J. Geophys. Res.,* **111,** C11S13, doi:10.1029/2005JC003203.

Liang, W.-D., T. Y. Tang, Y. J. Yang, M. T. Ko, and W.-S. Chuang, 2003: Upper-ocean currents around Taiwan. *Deep-Sea Res. II,* **50,** 1085–1105, doi:10.1016/S0967-0645(03)00011-0.

Liao, E., Y. Jiang, L. Li, H. Hong, and X. Yan, 2013: The cause of the 2008 cold disaster in the Taiwan Strait. *Ocean Modell.,* **62,** 1–10, doi:10.1016/j.ocemod.2012.11.004.

Lin, S. F., T. Y. Tang, S. Jan, and C.-J. Chen, 2005: Taiwan Strait current in winter. *Cont. Shelf Res.,* **25,** 1023–1042, doi:10.1016/j.csr.2004.12.008.

Lin, X.-H., L.-Y. Oey, and D.-P. Wang, 2007: Altimetry and drifter assimilations of Loop Current and eddies. *J. Geophys. Res.,* **112,** C05046, doi:10.1029/2006JC003779.

Liu, J. Y., 2013: Status of marine biodiversity of the China Seas. *PLoS ONE,* **8,** e50719, doi:10.1371/journal.pone.0050719.

Liu, K.-K., T.-H. Peng, P.-T. Shaw, and F. K. Shiah, 2003: Circulation and biogeochemical processes in the East China Sea and the vicinity of Taiwan: An overview and a brief synthesis. *Deep-Sea Res. II,* **50,** 1055–1064, doi:10.1016/S0967-0645(03)00009-2.

McCartney, M. S., 1975: Inertial Taylor columns on a beta plane. *J. Fluid Mech.,* **68,** 71–95, doi:10.1017/S0022112075000699.

Mertz, G., and D. G. Wright, 1992: Interpretations of the JEBAR term. *J. Phys. Oceanogr.,* **22,** 301–305, doi:10.1175/1520-0485(1992)022<0301:IOTJT>2.0.CO;2.

Ning, X., Z. Liu, Y. Cai, M. Fang, and F. Chai, 1998: Physicobiological oceanographic remote sensing of the East China Sea: Satellite and in situ observation. *J. Geophys. Res.,* **103** (C10), 21 623–21 635, doi:10.1029/98JC01612.

North, G. R., T. L. Bell, and R. F. Cahalan, 1982: Sampling errors in the estimation of empirical orthogonal functions. *Mon. Wea. Rev.,* **110,** 699–706, doi:10.1175/1520-0493(1982)110<0699:SEITEO>2.0.CO;2.

Oey, L.-Y., Y.-C. Hsin, and C.-R. Wu, 2010: Why does the Kuroshio northeast of Taiwan shift shelfward in winter? *Ocean Dyn.,* **60,** 413–426, doi:10.1007/s10236-009-0259-5.

——, M.-C. Chang, Y.-L. Chang, Y.-C. Lin, and F.-H. Xu, 2013a: Decadal warming of coastal China Seas and coupling with winter monsoon and currents. *Geophys. Res. Lett.,* **40,** 6288–6292, doi:10.1002/2013GL058202.

——, Y.-L. Chang, Y.-C. Lin, M.-C. Chang, F.-H. Xu, and H.-F. Lu, 2013b: ATOP—The Advanced Taiwan Ocean Prediction System based on the mpiPOM. Part 1: Model descriptions, analyses and results. *Terr. Atmos. Oceanic Sci.,* **24,** 137–158, doi:10.3319/TAO.2012.09.12.01(Oc).

Pan, A. J., X. F. Wan, X. G. Guo, and C. S. Jing, 2013: Responses of the Zhe-Min coastal current adjacent to Pingtan Island to the wintertime monsoon relaxation in 2006 and its mechanism. *Sci. China Earth Sci.,* **56,** 386–396, doi:10.1007/s11430-012-4429-9.

Pedlosky, J., 1979: *Geophysical Fluid Dynamics.* Springer-Verlag, 624 pp.

Salmon, R., 1992: A two-layer Gulf Stream over a continental slope. *J. Mar. Res.,* **50,** 341–365, doi:10.1357/002224092784797610.

Signell, R. P., and W. R. Geyer, 1991: Transient eddy formation around headlands. *J. Geophys. Res.,* **96** (C2), 2561–2575, doi:10.1029/90JC02029.

Voris, H. K., 2000: Maps of Pleistocene sea levels in Southeast Asia: Shorelines, river systems, time durations. *J. Biogeogr.,* **27,** 1153–1167, doi:10.1046/j.1365-2699.2000.00489.x.

Wang, R., T. Zuo, and K. Wang, 2003: The Yellow Sea cold bottom water—An oversummering site for *Calanus sinicus* (Copepoda, Crustacea). *J. Plankton Res.,* **25,** 169–183, doi:10.1093/plankt/25.2.169.

Wang, Y. H., S. Jan, and D. P. Wang, 2003: Transports and tidal current estimates in the Taiwan Strait from shipboard ADCP observations (1999–2001). *Estuarine Coastal Shelf Sci.,* **57,** 193–199, doi:10.1016/S0272-7714(02)00344-X.

Wu, C.-R., and Y.-C. Hsin, 2005: Volume transport through the Taiwan Strait: A numerical study. *Terr. Atmos. Oceanic Sci.,* **16,** 377–391.

——, S.-Y. Chao, and C. Hsu, 2007: Transient, seasonal and interannual variability of the Taiwan Strait Current. *J. Oceanogr.,* **63,** 821–833, doi:10.1007/s10872-007-0070-1.

Xu, F.-H., and L.-Y. Oey, 2011: The origin of along-shelf pressure gradient in the middle Atlantic bight. *J. Phys. Oceanogr.,* **41,** 1720–1740, doi:10.1175/2011JPO4589.1.

Yang, J., 2007: An oceanic current against the wind: How does Taiwan Island steer warm water into the East China Sea? *J. Phys. Oceanogr.,* **37,** 2563–2569, doi:10.1175/JPO3134.1.

Yu, H.-S., and Y.-W. Chou, 2001: Physiographic and geological characteristics of shelves in north and west of Taiwan. *Sci. China Earth Sci.,* **44,** 696–707.

Yu, T., Z. Deng, G. Han, X. Wu, H. Fu, and K. Wu, 2012: The reanalysis of currents and throughflow volume transport in the Taiwan Strait. *Mar. Geod.,* **35,** 16–31, doi:10.1080/01490419.2011.572765.

Zhang, G.-T., S. Sun, and B. Yang, 2007: Summer reproduction of the planktonic copepod *Calanus sinicus* in the Yellow Sea. *J. Plankton Res.,* **29,** 179–186, doi:10.1093/plankt/fbm005.